International Journal of Solids and Structures 199 (2020) 190–202

Contents lists available at ScienceDirect

International Journal of Solids and Structures

journal homepage: www.elsevier.com/locate/ijsolstr

Fracture mechanisms in largely strained solids due to surface instabilities

Borja Erice[a,b,*], María Jesús Pérez-Martín[a,b], Martin Kristoffersen[a,b], David Morin[a,b], Tore Børvik[a,b], Odd Sture Hopperstad[a,b]

[a] Structural Impact Laboratory (SIMLab), Department of Structural Engineering, Norwegian University of Science and Technology (NTNU), NO-7491 Trondheim, Norway
[b] Centre for Advanced Structural Analysis (CASA), NTNU, NO-7491 Trondheim, Norway

ARTICLE INFO

Article history:
Received 10 March 2020
Revised 27 March 2020
Accepted 3 April 2020
Available online 15 May 2020

Keywords:
Bifurcation analysis
Crease formation
Porous plasticity
Ductile-to-brittle transition

ABSTRACT

The effect of self-contacting surface defects generated by largely compressing metals on the ductile-to-brittle transition observed in metallic structures is investigated. In order to analyse such an effect, a finite element model of a half-space plane-strain material block with an imperfection was subjected to different levels of compression followed by reverse tensile straining. Experimentally validated associative J_2 and porous plasticity models were used to describe the mechanical response of the pipeline steel employed as a baseline material for this investigation. Both models predicted onset of creasing at compressive strains of around 70%. To ascertain whether the creases created large and sharp enough defects to trigger the ductile-to-brittle transition during the tensile straining phase, a bifurcation analysis implemented within a user material subroutine was used as fracture initiation indicator. This confirmed that at compressive strains above 70% the self-contact defect acted as a crack during the tensile straining phase.

1. Introduction

Wrinkles can be found on the surface of largely compressed areas of metallic materials such as the compressive side of components subjected to bending actions. These surface instabilities can be observed in structural elements that are of interest for the automotive and offshore industries, such as bent tubes or pipes, pressure vessels or die formed sheet metal pieces. Here, wrinkles are understood as undulations or surface roughness that might set in due to large straining in metallic materials. Typically, they present distinct geometrical features that are periodically repeated on the surface and they are dimension-wise significantly smaller than any of the dimensions that define the rest of the solid. They fold and self-contact when the structural elements are increasingly strained remotely. An example of such wrinkles can be observed in Fig. 1, which shows an optical micrography obtained from the compression side of a quasi-static three-point pipe bending test conducted on X65 steel (Kristoffersen et al. (2016b)). The details of the specimen that the micrograph was taken from and the testing conditions are described in Section 3.2. The formation of instabilities on the compressive side or "concave" part of solids subjected to bending loads was already pointed out by Triantafyllidis et al. (1982). Eventually, the self-contact grows unsteadily evolving into a crease, a specific type of singularity. Therefore, the onset of a crease formation can be detected when the self-contact length grows unsteadily. This phenomenon by itself may not pose any threat to the structural integrity of the solid. However, the formation of a crease can develop into a surface crack that might lead to catastrophic failure when unloading or further reverse straining such solid. Hence, this phenomenon is important to consider in industrial applications when surface imperfections such as wrinkles are detected.

The onset of wrinkling as a surface instability when elastomeric materials are compressed is a phenomenon that has been previously studied (Gent and Cho (1999); Cao and Hutchinson (2012a); Lihua (2014)). Similar studies on bi-layered solids representing artificial substrate-film systems (Cao and Hutchinson (2012b); Budday et al. (2017)) or biological tissues such as the mucosa–submucosa systems (Li et al. (2011a); Li et al. (2011b)) have also been performed. The development of surface instabilities has also been studied for metallic materials. Instability creation in traction-free surfaces was investigated numerically using half-space unit cell finite element (FE) models that employed a smooth and corner-type (Christoffersen and Hutchinson (1979)) J_2 plastic-

* Corresponding author.
E-mail address: borja.erice@ntnu.no (B. Erice).

https://doi.org/10.1016/j.ijsolstr.2020.04.008

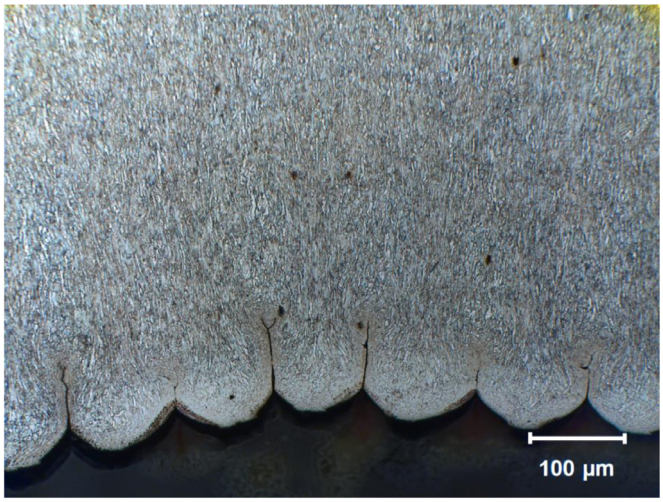

Fig. 1. Compressive side of the same three-point pipe bending test performed on X65 steel (reproduced from Kristoffersen (2014)).

ity by Hutchinson and Tvergaard (1980). Using a similar unit cell model, Legarth and Richelsen (2006) studied the effect of the plastic flow, and smooth isotropic and anisotropic yield surfaces on the surface instability formation. In this investigation, the wrinkle or surface instability formation is not the main subject of study and will therefore not be covered. However, the readers are referred to

Crease formation has been widely studied in soft elastomers (Mora et al. (2011); Hohlfeld and Mahadevan (2012)), biological materials such as tissues (Jin et al. (2011); Stewart et al. (2016)) and hydrogels (Trujillo et al. (2008); Hong et al. (2009); Yoon et al. (2010)) amongst others. However, there is not much literature devoted to crease formation in metallic materials (Yang et al. (2019)). Based on previous ideas that Cao and Hutchinson (2012b) or Hohlfeld and Mahadevan (2012) employed for different materials, Yang et al. (2019) performed FE simulations on a solid plane strain block with J_2 plasticity and linear work hardening that had an artificial surface defect orders of magnitude smaller than the block dimensions. According to this recent and unique study of crease formation in metals, the onset of creasing was strongly influenced by the plasticity of the material, retarding its formation. More specifically, they observed that for larger values of E_t/E, being E and E_t the elastic and tangent linear moduli respectively, smaller compressive strains were needed to generate a crease in the material. However, the range of studied E_t/E values, from 0.08 to 0.75, is far from real work hardening characteristics of most metallic alloys.

The objective of the present investigation is twofold: (i) to determine the critical strain for the onset of crease formation for ductile solids and (ii) to assess if the formation of creases due to the self-contact eventually transforms into a defect capable of leading to a brittle catastrophic failure. This latter phenomenon will cause a ductile-to-brittle fracture transition due to surface defects. X65 pipe steel, previously studied and characterised in detail by Kristoffersen et al. (2013); Kristoffersen et al. (2014), has been used as a base material for the present study.

Inspired by the results from Yang et al. (2019), FE simulations of a plane-strain block with a surface imperfection subjected to different levels of increasing compressive strains have been carried out with calibrated J_2-based metal and porous plasticity models of the X65 pipe steel to determine the critical strain for crease formation. To ascertain if the folded self-contacting defects generated in the crease formation process pose a threat for the structural integrity of the solid, a reverse tensile strain has been prescribed in the block and the stress state on the tip of the defect has been analysed. To further evaluate if the geometry of such a defect will eventually produce a brittle failure, virtually behaving like a crack, a strain localisation criterion has been implemented in the material level user subroutine of the porous plasticity model allowing the detection of inhomogeneous strain states within a finite element. Following Rice (1976), and as indicated in Morin et al. (2018), the implementation has been carried out performing a bifurcation analysis and getting the strain localisation indicator from the condition of loss of ellipticity. For this particular material a critical compressive engineering strain of 70% was detected. Furthermore, the study showed that for compressive strains above such critical strain, the lengths of the self-contacting defects generated in the compression phase were large enough to act like cracks causing the material to fracture in a brittle manner during the tensile loading.

2. Porous plasticity model

2.1. Constitutive equations

The constitutive equations have been formulated using a corotational formulation where we define the following transformations of the Cauchy stress and rate-of-deformation tensors,

$$\widehat{\boldsymbol{\sigma}} = \mathfrak{R}^T \cdot \boldsymbol{\sigma} \cdot \mathfrak{R} \text{ and } \widehat{\mathbf{D}} = \mathfrak{R}^T \cdot \mathbf{D} \cdot \mathfrak{R} \tag{1}$$

where $\mathfrak{R}$ is an orthogonal tensor, i.e. $\mathfrak{R}^{-1} = \mathfrak{R}^T$, that transforms the tensor components between the fixed, global and a corotational, local coordinate systems. The local material coordinate system evolves according to $\dot{\mathfrak{R}} = \mathbf{W} \cdot \mathfrak{R}$, where $\mathbf{W}$ is the spin tensor and the rotation tensor has an initial value of $\mathfrak{R}|_{t=0} = \mathbf{I}$ where $(\mathbf{I})_{ij} = \delta_{ij}$ is the second-order unit tensor.

We assume the additive decomposition of the rate-of-deformation tensor as:

$$\hat{\mathbf{D}} = \hat{\mathbf{D}}^e + \hat{\mathbf{D}}^p \tag{2}$$

where $\hat{\mathbf{D}}^e$ and $\hat{\mathbf{D}}^p$ are the elastic and plastic parts of the corotational rate-of-deformation tensor respectively. The rate form of the linear elastic isotropic law is then defined as:

$$\dot{\hat{\boldsymbol{\sigma}}} = \hat{\mathbb{C}} : \hat{\mathbf{D}}^e = \hat{\mathbb{C}} : \left(\hat{\mathbf{D}} - \hat{\mathbf{D}}^p\right) \tag{3}$$

being $\hat{\mathbb{C}}$ the symmetric fourth-order tensor that contains the shear G and the bulk K moduli in the following form:

$$\hat{\mathbb{C}} = 2G\mathbb{I}' + K\mathbf{I} \otimes \mathbf{I} \tag{4}$$

with $G = E/(2+2\nu)$ and $K = E/(3-6\nu)$ that contain the elastic modulus E and the Poisson's ratio ν. The symmetric fourth-order deviatoric unit tensor, $\mathbb{I}' = \mathbb{I}_S - 1/3(\mathbf{I} \otimes \mathbf{I})$ is defined with the symmetric fourth-order unit tensor, $(\mathbb{I}_S)_{ijkl} = 1/2(\delta_{ik}\delta_{jl} + \delta_{il}\delta_{jk})$ and the tensor $(\mathbf{I}\otimes\mathbf{I})_{ijkl} = \delta_{ij}\delta_{kl}$. The main advantage of choosing the corotational formulation is that the stress rate $\dot{\hat{\boldsymbol{\sigma}}}$ is an objective tensor.

The function chosen to describe the plastic yielding of the porous solid, first introduced by Gurson (1977) and later modified by Tvergaard (1981), is given by:

$$\phi\left[\hat{\boldsymbol{\sigma}}, \mathbf{a}\right] = \frac{\overline{\sigma}^2}{\sigma_{\mathrm{m}}^2} + 2q_1 f \cosh\left[\frac{3}{2} q_2 \frac{\sigma_{\mathrm{h}}}{\sigma_{\mathrm{m}}}\right] - 1 - q_1^2 f^2 = 0 \tag{5}$$

where q_1 and q_2 are the so-called Tvergaard constants, $\overline{\sigma} = \sqrt{3/2\hat{\boldsymbol{\sigma}}' : \hat{\boldsymbol{\sigma}}'}$ is the macroscopic von Mises stress, $\sigma_{\mathrm{h}} = \mathrm{tr}[\hat{\boldsymbol{\sigma}}]/3$ is the hydrostatic stress, $\hat{\boldsymbol{\sigma}}' = \hat{\boldsymbol{\sigma}} - \sigma_{\mathrm{h}}\mathbf{I}$ is the deviatoric part of the corotational Cauchy stress tensor, σ_{m} is the flow stress of the matrix material, and $\mathbf{a} = \{\overline{\varepsilon}_p \ f\}^T$ is the vector that contains the internal variables: the equivalent plastic strain $\bar{\varepsilon}_p$ and the void volume fraction f. The classical von Mises (or J_2) associative plasticity is recovered if the void volume fraction is zero and it does not evolve with any of the internal variables.

For the sake of simplicity, the matrix hardening is considered isotropic and it is defined with the following law:

$$\sigma_{\mathrm{m}}[\bar{\varepsilon}_p] = \sigma_0 + B\bar{\varepsilon}_p^n + \sum_{i=1}^{2} Q_i(1 - \exp[-C_i\bar{\varepsilon}_p]) \tag{6}$$

where σ_0 is the yield stress, B and n are the constants of the power-law hardening and Q_1,C_1,Q_2,$C_2$are the constants of the two-term Voce work hardening law.

The flow rule is associative, which leads to the following form of the plastic corotational rate-of-deformation tensor,

$$\widehat{\mathbf{D}}^p = \dot{\lambda}\frac{\partial\phi}{\partial\hat{\boldsymbol{\sigma}}} = \dot{\lambda}\widehat{\mathbf{N}} \tag{7}$$

where the flow vector $\mathbf{N}$ is calculated as:

$$\widehat{\mathbf{N}} = \frac{\partial\phi}{\partial\hat{\boldsymbol{\sigma}}} = \frac{3}{\sigma_{\mathrm{m}}^2}\hat{\boldsymbol{\sigma}}' + \frac{q_1q_2f}{\sigma_{\mathrm{m}}}\sinh\left[\frac{3}{2}q_2\frac{\sigma_{\mathrm{h}}}{\sigma_{\mathrm{m}}}\right]\mathbf{I} \tag{8}$$

Note that due to its form, the flow vector can also be additively decomposed into a deviatoric ($\widehat{\mathbf{N}}'$) and a volumetric ($\widehat{\mathbf{N}}_{\mathrm{v}}$) part that are directly related to the corresponding parts of the corotational rate-of-deformation tensor such that,

$$\widehat{\mathbf{D}}^p = \widehat{\mathbf{D}}'^{\mathbf{p}} + \widehat{\mathbf{D}}_{\mathrm{v}}^p = \widehat{\mathbf{D}}'^{\mathbf{p}} + \frac{1}{3}\hat{D}_{\mathrm{v}}^p\mathbf{I} = \dot{\lambda}\left(\widehat{\mathbf{N}}' + \frac{1}{3}\hat{N}_{\mathrm{v}}\mathbf{I}\right) \tag{9}$$

Therefore, the deviatoric/volumetric split of the corotational rate-of-deformation tensor is fully defined by:

$$\widehat{\mathbf{N}}' = \mathrm{dev}\left[\mathbf{N}'\right] = \frac{3}{\sigma_{\mathrm{m}}^2}\hat{\boldsymbol{\sigma}}' \tag{10}$$

$$\hat{N}_{\mathrm{v}} = \mathrm{tr}\left[\widehat{\mathbf{N}}\right] = \frac{3q_1q_2f}{\sigma_{\mathrm{m}}}\sinh\left[\frac{3}{2}q_2\frac{\sigma_{\mathrm{h}}}{\sigma_{\mathrm{m}}}\right] \tag{11}$$

The evolution of the hardening variables $\dot{\mathbf{a}}$ is given by the hardening moduli $\mathbf{h} = \{h_\varepsilon h_f\}^T$ as,

$$\dot{\mathbf{a}} = \dot{\lambda}\mathbf{h} \tag{12}$$

Operating on the work conjugacy, i.e.,

$$\hat{\boldsymbol{\sigma}} : \widehat{\mathbf{D}}^p = (1-f)\sigma_{\mathrm{m}}\dot{\bar{\varepsilon}}_p \tag{13}$$

the evolution equation of the equivalent plastic strain as a function of the plastic multiplier $\dot{\lambda}$ is obtained as,

$$\dot{\bar{\varepsilon}}_p = \dot{\lambda}h_\varepsilon = \dot{\lambda}\frac{\hat{\boldsymbol{\sigma}} : \widehat{\mathbf{N}}}{(1-f)\sigma_{\mathrm{m}}} \text{ being } \bar{\varepsilon}_p = \int \dot{\bar{\varepsilon}}_p dt \tag{14}$$

The void volume fraction evolution is defined by combining strain-based void nucleation ($\dot{f}_n$) and void growth ($\dot{f}_g$) terms. The former is based on the rate of change of the equivalent plastic strain, whereas the latter is related to the volumetric growth of the plastic strain as:

$$\dot{f} = \dot{f}_n + \dot{f}_g = \dot{\lambda}h_f = A_n\dot{\bar{\varepsilon}}_p + (1-f)\hat{D}_{\mathrm{v}}^p = \dot{\lambda}\{A_nh_\varepsilon + (1-f)N_{\mathrm{v}}\} \tag{15}$$

where A_n is a material parameter.

The loading/unloading conditions are stated in Kuhn-Tucker form as:

$$\phi \le 0, \dot{\lambda} \ge 0, \dot{\lambda}\phi = 0 \tag{16}$$

From the consistency condition ($\dot{\phi} = 0$) for plastic flow ($\dot{\lambda} > 0$), the yield function is differentiated in terms of the corotational Cauchy stress $\hat{\boldsymbol{\sigma}}$ and the internal variables $\mathbf{a}$, leading to the following non-linear equation in $\dot{\lambda}$,

$$\dot{\phi} = \frac{\partial\phi}{\partial\hat{\boldsymbol{\sigma}}} : \dot{\hat{\boldsymbol{\sigma}}} + \frac{\partial\phi}{\partial\mathbf{a}}\cdot\dot{\mathbf{a}} = \widehat{\mathbf{N}} : \widehat{\mathbb{C}} : \widehat{\mathbf{D}} - \dot{\lambda}\widehat{\mathbf{N}} : \widehat{\mathbb{C}} : \widehat{\mathbf{N}} + \dot{\lambda}\mathbf{f_a}\cdot\mathbf{h} = 0 \tag{17}$$

where the components of $\mathbf{f_a} = \partial\phi/\partial\mathbf{a} = \{\phi_\varepsilon\phi_f\}^T$ are:

$$\begin{aligned}\phi_\varepsilon &= \frac{\partial\phi}{\partial\bar{\varepsilon}_p} = -\left(2\frac{\bar{\sigma}^2}{\sigma_{\mathrm{m}}^3} + 3q_1q_2f\frac{\sigma_{\mathrm{h}}}{\sigma_{\mathrm{m}}^2}\sinh\left[\frac{3}{2}q_2\frac{\sigma_{\mathrm{h}}}{\sigma_{\mathrm{m}}}\right]\right)\\ &\left(Bn\bar{\varepsilon}_p^{n-1} + \sum_{i=1}^{2}Q_iC_i\exp[-C_i\bar{\varepsilon}_p]\right)\\ \phi_f &= \frac{\partial\phi}{\partial f} = 2q_1\cosh\left[\frac{3}{2}q_2\frac{\sigma_{\mathrm{h}}}{\sigma_{\mathrm{m}}}\right] - 2q_1^2f\end{aligned} \tag{18}$$

From eq. (17) we can explicitly obtain the plastic multiplier:

$$\dot{\lambda} = \frac{\widehat{\mathbf{N}} : \widehat{\mathbb{C}} : \widehat{\mathbf{D}}}{\widehat{\mathbf{N}} : \widehat{\mathbb{C}} : \widehat{\mathbf{N}} - \mathbf{f_a}\cdot\mathbf{h}} \tag{19}$$

Substituting eq. (19) in eq. (3) and operating we get:

$$\dot{\hat{\boldsymbol{\sigma}}} = \widehat{\mathbb{C}}^{ep} : \widehat{\mathbf{D}} = \widehat{\mathbb{C}} : \widehat{\mathbf{D}} - \dot{\lambda}\widehat{\mathbb{C}} : \widehat{\mathbf{N}} \Rightarrow \widehat{\mathbb{C}}^{ep} = \widehat{\mathbb{C}} - \frac{\widehat{\mathbf{P}}\otimes\widehat{\mathbf{P}}}{\widehat{\mathbf{N}} : \widehat{\mathbb{C}} : \widehat{\mathbf{N}} - \mathbf{f_a}\cdot\mathbf{h}} \tag{20}$$

where $\widehat{\mathbf{P}} = \widehat{\mathbb{C}} : \widehat{\mathbf{N}} = 2G\widehat{\mathbf{N}}' + K\hat{N}_{\mathrm{v}}\mathbf{I}$. This allows to define a direct relationship between the total rate-of-deformation and the rate of the corotational Cauchy stress tensors given by the continuum tangent modulus $\widehat{\mathbb{C}}^{ep}$.

To express the rate constitutive equations in the fixed, global coordinate system, the Jaumann rate of the Cauchy stress tensor $\boldsymbol{\sigma}^\nabla$ is defined as:

$$\boldsymbol{\sigma}^\nabla = \dot{\boldsymbol{\sigma}} - \mathbf{W}\cdot\boldsymbol{\sigma} + \boldsymbol{\sigma}\cdot\mathbf{W} = \mathfrak{R}\cdot\dot{\hat{\boldsymbol{\sigma}}}\cdot\mathfrak{R}^T \tag{21}$$

The rate constitutive equations are then obtained in the form:

$$\dot{\boldsymbol{\sigma}} = \mathbb{C}^{ep} : \mathbf{D} + \mathbf{W}\cdot\boldsymbol{\sigma} - \boldsymbol{\sigma}\cdot\mathbf{W} \tag{22}$$

where the components of $\mathbb{C}^{ep}$in the fixed, global coordinate system are expressed as:

$$\left(\mathbb{C}^{ep}\right)_{ijkl} = \mathfrak{R}_{im}\mathfrak{R}_{jn}\mathfrak{R}_{kp}\mathfrak{R}_{lq}\left(\widehat{\mathbb{C}}^{ep}\right)_{mnpq} \tag{23}$$

The constitutive model equations were implemented in their incremental form as a user material subroutine in the LS-DYNA nonlinear explicit time integration FE solver.

In this study, we will consider strain localisation by loss of ellipticity as an indicator for material failure. The condition for a continuous bifurcation in an elastic-plastic solid where a discontinuity of the velocity gradient field across a planar band with normal $\mathbf{n}$ becomes possible, as illustrated in Fig. 2(a), was derived by Rice (1976) and Rice and Rudnicki (1980). Assuming plastic loading both outside and inside of the band, the condition for bifurcation is given by

$$\det[\mathbf{A}] = 0 \tag{24}$$

where the acoustic tensor $\mathbf{A}$is defined as

$$\mathbf{A}[\mathbf{n}] = \mathbf{n}\cdot\mathbb{C}^{ep}\cdot\mathbf{n} + \mathbf{R} \tag{25}$$

with

$$2\mathbf{R} = -\mathbf{n}\otimes(\mathbf{n}\cdot\boldsymbol{\sigma}) + (\mathbf{n}\cdot\boldsymbol{\sigma})\otimes\mathbf{n} + (\mathbf{n}\cdot\boldsymbol{\sigma}\cdot\mathbf{n})\mathbf{I} - \boldsymbol{\sigma} \tag{26}$$

This is a necessary condition for the loss of ellipticity. As pointed out by Rudnicki and Rice (1975) we assume the planar band normal to be contained in the plane defined by the maximum and minimum principal stress directions $\mathbf{e}_I$ and $\mathbf{e}_{III}$ respectively as shown in Fig. 2(b), where the indices can be correlated with the principal stresses $\sigma_I \ge \sigma_{II} \ge \sigma_{III}$. This allows to define the normal with a single angle ϕ defined between the band normal $\mathbf{n}_\phi$ and the maximum principal direction $\mathbf{e}_I$ that can take values from $0 \le \varphi \le \pi/2$. To find the band normal with the condition min[det[$\mathbf{A}[\mathbf{n}_\phi]$]], an identical numerical procedure as that detailed in Morin et al. (2018) is followed. Other approaches such as the geometric close-form solutions proposed by Benallal and

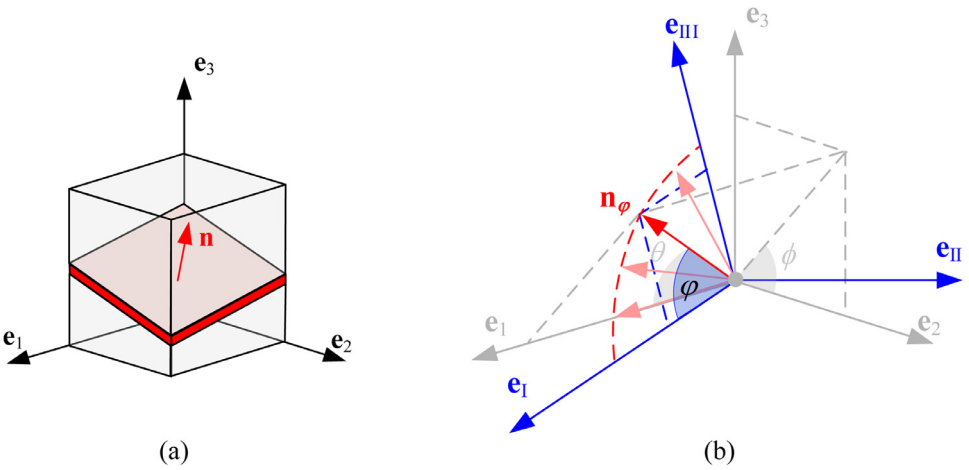

Fig. 2. Illustration of the planar band where all deformation is concentrated at onset of localisation causing non-homogeneous velocity gradient fields.

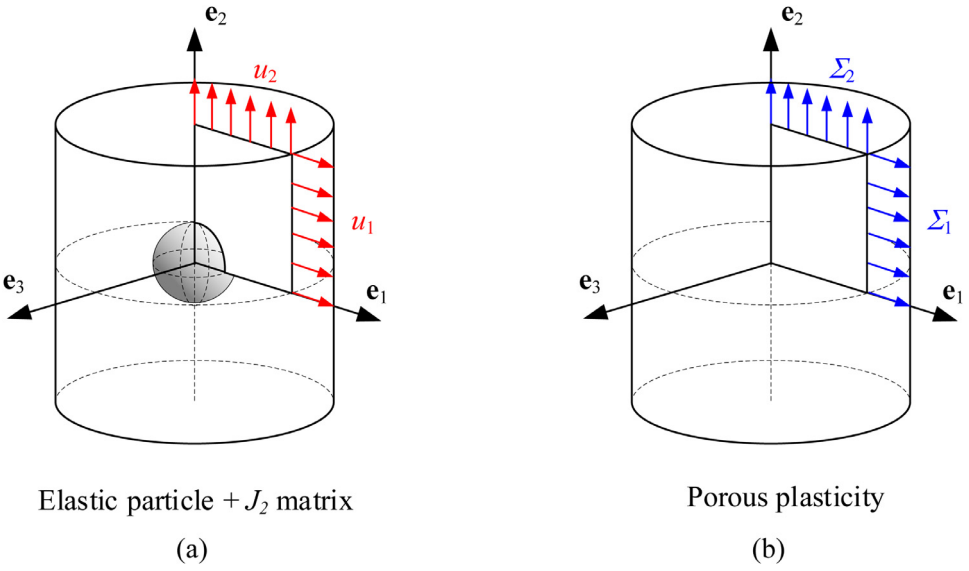

Fig. 3. Sketch of the axisymmetric unit cell with J_2 plasticity matrix that contains an elastic particle (a) and the axisymmetric element with the porous plasticity model (b), both subjected to proportional loadings.

Comi (1996) or Oliver and Huespe (2004) could be used to obtain the band orientation. The bifurcation criterion has been implemented together with the material model for porous media in a user material subroutine in the LS-DYNA non-linear explicit time integration FE solver.

2.2. Parameter identification

The elastic properties, $E = 208$ GPa and $\nu = 0.3$, and yield stress $\sigma_0 = 465.5$ MPa, were obtained from the mechanical tests on an X65 pipe steel reported in Kristoffersen et al. (2014). The yield function parameter q_1, was chosen to be $q_1 = 1.5$, a very widely employed constant in the literature based on Tvergaard (1981). The mechanical response of a unit cell containing the relevant features of the material was used to calibrate the remaining yield function constant q_2, the two-term Voce isotropic hardening parameters Q_1,C_1,Q_2,C_2 ($B = 0$), and the strain-based void nucleation coefficient A_n.

Taking advantage of the material symmetry allowed to model only half of an axisymmetric unit cell of initial height H_0 and initial radius R_0 that was composed by a linear elastic particle of initial radius r_0 and elastic modulus of $E = 208$ GPa embedded in an elastic-plastic matrix (see Fig. 3(a)) that was modelled using associative J_2 plasticity with isotropic hardening calibrated in Kristoffersen et al. (2016a) (see Table 1). The initial void volume fraction and size of the particles were measured and found out to be $f_0 = 2r_0^3/(3R_0^2H_0) = 0.0005$ and $r_0 = 25$ μm, respectively, as shown in Kristoffersen et al. (2016a). Henceforth, the term f will contain the combined volume fraction of both void and particle.

Table 1
Strain hardening constants for the porous and von Mises plasticity models corresponding to the X65 pipe steel.

Strain hardening				
Porous plasticity				
B[MPa]	Q_1[MPa]	C_1	Q_2[MPa]	C_2
0.00	130.00	26.46	350.00	0.87
J_2 plasticity (after Kristoffersen et al. (2014))				
B[MPa]	n		Q_1[MPa]	Q_2[MPa]
410.8	0.4793		0.0	0.0

The cylindrical strain state that the unit cell is subjected to is reflected in the form of the macroscopic logarithmic strain tensor:

$$\mathbf{E} = E_1(\mathbf{e}_1 \otimes \mathbf{e}_1 + \mathbf{e}_3 \otimes \mathbf{e}_3) + E_2\mathbf{e}_2 \otimes \mathbf{e}_2 \tag{27}$$

where its components E_1 and E_2 are calculated as follow:

$$E_1 = \ln\left[\frac{R}{R_0}\right] \text{and} \, E_2 = \ln\left[\frac{H}{H_0}\right] \tag{28}$$

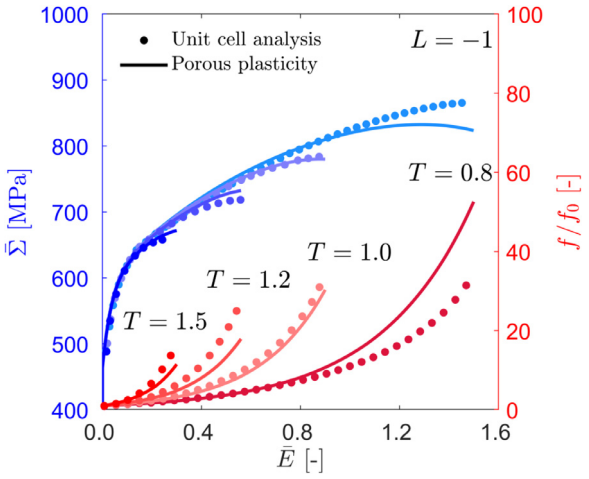

Fig. 4. Macroscopic equivalent stress-strain curves (in blue) and normalised combined void and particle volume fraction against macroscopic equivalent strain (in red) for triaxialities of $T = [0.8, 1.0, 1.2, 1.5]$ and Lode angle parameter of $L = -1$. Dots indicate the results from the unit cell analysis, while the solid lines are the numerical simulations using the porous plasticity model.

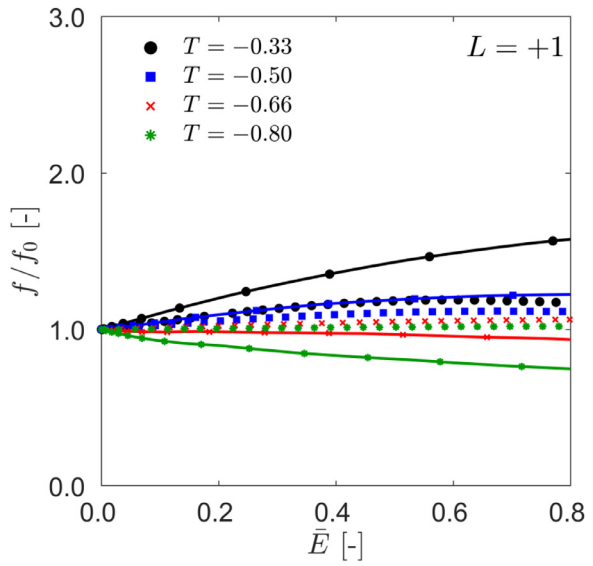

Fig. 5. Normalised combined void and particle volume fraction against macroscopic equivalent strain with triaxialities of $T = [-0.33, -0.50, -0.66, -0.80]$ and Lode angle parameter of $L = +1$. Symbols indicate the results from the unit cell analysis, while the solid lines with symbols correspond to the numerical simulations using the porous plasticity model.

Here, $R = R_0 + u_1$ and $H = H_0 + u_2$ are the deformed components of the unit cell's radius and height, respectively. The equivalent macroscopic strain is defined with the macroscopic logarithmic strain tensor:

$$\bar{E} = \sqrt{\frac{2}{3}\mathbf{E}' : \mathbf{E}'} = \frac{2}{3}|E_2 - E_1| \tag{29}$$

The macroscopic Cauchy stress tensor components are defined as the work conjugates of their respective strain components giving the following tensor:

$$\boldsymbol{\Sigma} = \Sigma_1(\mathbf{e}_1 \otimes \mathbf{e}_1 + \mathbf{e}_3 \otimes \mathbf{e}_3) + \Sigma_2 \mathbf{e}_2 \otimes \mathbf{e}_2 \tag{30}$$

where its components are:

$$\Sigma_1 = \frac{P_1}{2\pi RH} \text{ and } \Sigma_2 = \frac{P_2}{\pi R^2} \tag{31}$$

P_1 and P_2 are the tractions integrated over the planes with normals $\mathbf{e}_1$ and $\mathbf{e}_2$ respectively.

The macroscopic stress state of the axisymmetric unit cell is defined by the macroscopic von Mises stress $\bar{\Sigma}$, the stress triaxiality T and the Lode angle parameter L with:

$$\begin{aligned}\bar{\Sigma} &= \sqrt{\frac{3}{2}\boldsymbol{\Sigma}' : \boldsymbol{\Sigma}'} = |\Sigma_2 - \Sigma_1|,\ T = \frac{\Sigma_h}{\bar{\Sigma}} \\ &= \frac{2\Sigma_1 + \Sigma_2}{3|\Sigma_2 - \Sigma_1|},\ L = \frac{2\Sigma_{II} - \Sigma_I - \Sigma_{III}}{\Sigma_I - \Sigma_{III}}\end{aligned} \tag{32}$$

where $L = -1$ for axisymmetric tension ($\Sigma_I = \Sigma_2, \Sigma_{II} = \Sigma_{III} = \Sigma_1$) and $L = +1$ for axisymmetric compression ($\Sigma_I = \Sigma_{II} = \Sigma_1, \Sigma_{III} = \Sigma_2$).

The unit cell simulations were performed employing the ABAQUS/Standard implicit time integration solver under displacement-controlled boundary conditions, while values of the macroscopic stress triaxiality and the Lode angle parameter were prescribed. The methodology and procedure to perform such simulations has been successfully used by other authors in the past, e.g. Faleskog et al. (1998), and more details about it can be found in the work by Dæhli et al. (2016). Unit cell simulations in axisymmetric tension ($L = -1$) were carried out for macroscopic stress triaxialities of $T = [0.8, 1.0, 1.2, 1.5]$ (see Fig. 4). Since the parameter f is considered as the combined void and particle volume fraction, henceforth referred to as the combined volume fraction, it was of interest observing the response of the unit cell under stress states which could cause anomalous effects for the type of material model described in the previous section, i.e. the absence of voids collapsing. Therefore, unit cell simulations in axisymmetric compression ($L = +1$) were performed for macroscopic stress triaxialities of $T = [-0.33, -0.50, -0.66, -0.80]$. As observed in Fig. 5, the combined volume fraction increases with increasing macroscopic equivalent strain until a global maximum was reached. This maximum varied depending on the triaxiality imposed on the unit cell. After the maximum, it decreased to almost the initial combined volume fraction.

To calibrate the constitutive model, single axisymmetric element simulations with prescribed pressure boundary conditions that contained the porous plasticity material model described in the Section 2.1 above were carried out using the LS-DYNA nonlinear explicit time integration FE solver as illustrated in Fig. 3(b). The initial combined volume fraction was set to $f_0 = 0.0005$ as in the unit cell simulations. The combined volume fraction evolution curves (see Figs. 4 and 5) from all the unit cell simulations were employed as targets in an iterative domain-reduction scheme for obtaining the material constants using the LS-OPT software package. As a result, a second yield function constant of $q_2 = 0.92$ and a strain-based nucleation coefficient of $A_n = 9.13{\cdot}10^{-4}$ combined with the strain hardening constants reported in Table 1 were found to give a more than reasonable fit as will be discussed subsequently. The strain-based nucleation was applied until a maximum value of combined volume fraction of $f = 0.001$ was reached.

The numerical results are shown as solid lines in Figs. 4 and 5 for the tensile ($L = -1$) and compressive ($L = +1$) cases respectively. The porous plasticity model results for the tensile loading were in good agreement for larger triaxialities, i.e. T equals 1.5, 1.2 and 1.0, while the lowest triaxiality case deviated from the unit cell results for macroscopic equivalent strains above 1.0. The simulations performed for the compressive case shown in Fig. 5 are in reasonable agreement with the unit cell simulations, capturing the general trend and, more importantly, avoiding the combined volume fraction to deviate excessively from the initial value. However, it should be emphasised that the void nucleation is a purely phenomenological artefact whose sole purpose is to avoid the com-

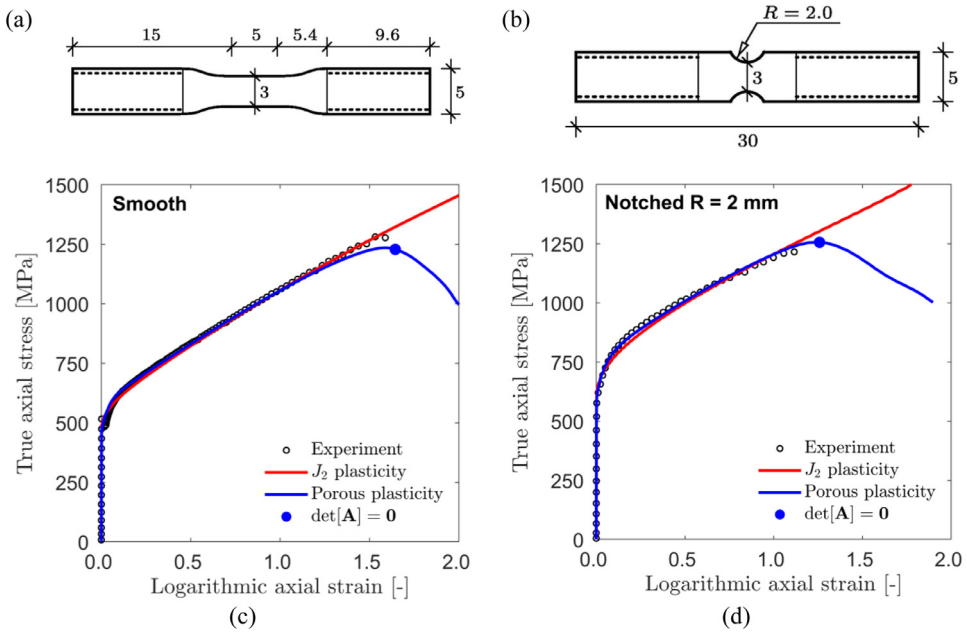

Fig. 6. Geometry and dimensions in mm of the smooth (a) and notched (c) tensile specimens. Numerical simulations of axisymmetric smooth (c) and notched (d) tensile specimens loaded under quasi-static conditions employing J2 (red) and porous plasticity (blue) models calibrated for the X65 pipe steel compared against the experimental data (hollow black circles) from Kristoffersen et al. (2016a).

bined volume fraction to deviate unreasonably from its initial value under compressive loads.

3. Model validation

To check the predictive capabilities of the calibrated porous plasticity model with the built-in bifurcation analysis, two types of quasi-static tests were simulated: tensile tests on smooth and notched specimens, and a three-point bending pipe test. For the sake of comparison, all tests were also simulated employing a standard J_2 plasticity model with isotropic hardening. The material constants for this model are summarised in Table 1, and the calibration procedure is reported in Kristoffersen et al. (2014).

3.1. Tensile tests

In the tensile tests with specimen geometries shown in Fig. 6(a) and (b), previously performed by Kristoffersen et al. (2016a), the true axial stress σ and the true axial strain ε were obtained from:

$$\sigma = \frac{F}{\pi\,(d/2)^2} \text{ and } \varepsilon = 2\ln\left[\frac{D}{d}\right] \tag{33}$$

where F is the force measured with the load cell, and D and d are the initial and the minimum cross-section diameters measured with a laser-based measuring device. The readers are referred to Kristoffersen et al. (2016a) for additional details on the experiments.

Using the specimen symmetries, only half of the geometries were discretised using 0.05 mm × 0.05 mm four-node single-integration-point axisymmetric elements with stiffness-based hourglass control. The experimentally measured velocities were prescribed on the nodes of one end, while the same degree of freedom was constrained on the nodes of the opposite end. A mass scaled solution with a stable time increment that provided 10^5 increments over the total time was employed. The reaction forces on these nodes and the minimum cross-section diameter were monitored to compute the axial true stress-strain curves shown in Fig. 6(c) and (d).

The axial true stress-strain response of both specimens was accurately described by both the J_2 and the porous plasticity models as show in Fig. 6(c) and (d). For both specimens, the bifurcation indicator predicted the onset of localisation to develop at the element located in the centre of the minimum cross-section. In Fig. 6(c) and (d), a blue dot indicates the precise moment when the bifurcation indicator first computed a negative det[**A**] for a certain band orientation. The predictions of the bifurcation indicator are in very good agreement with the experiments, giving an excellent estimation for the onset of material failure.

3.2. Three-point pipe bending test

A quasi-static three-point bending test on a pipe with geometry and dimension depicted in Fig. 7(a) and reported as "Q2" by Kristoffersen et al. (2016b) was simulated to validate the porous plasticity model at the component level. The force measurements were gathered from the load cell that the indenter was attached to, whereas the displacement was obtained from the cross-head position. The resulting force displacement curve is plotted in Fig. 7(c).

Only half of the component and the set-up was modelled making use of the pipe symmetry as it can be seen in the FE model shown in Fig. 7(b). The geometry was discretised with eight-node single-integration-point elements with stiffness-based hourglass control. The element size was progressively reduced, starting from the edges to the centre where a minimum element size of around 0.5 mm × 0.5 mm × 0.5 mm was employed. The cylindrical supports and indenter were modelled as rigid bodies. A prescribed constant velocity of 10 mm/min was imposed on the latter. A mass scaled solution with a stable time increment that provided $5{\cdot}10^5$ increments over the total time was employed. The forces were computed from the contact forces between the indenter and the pipe, while the displacement was directly obtained from the rigid body movement of the indenter. The geometry of the specimen after being tested (see Fig. 7(a)) was compared against the numerical simulations showing a very good agreement.

The force-displacement response from the numerical simulations using the J_2 and the porous plasticity models is compared

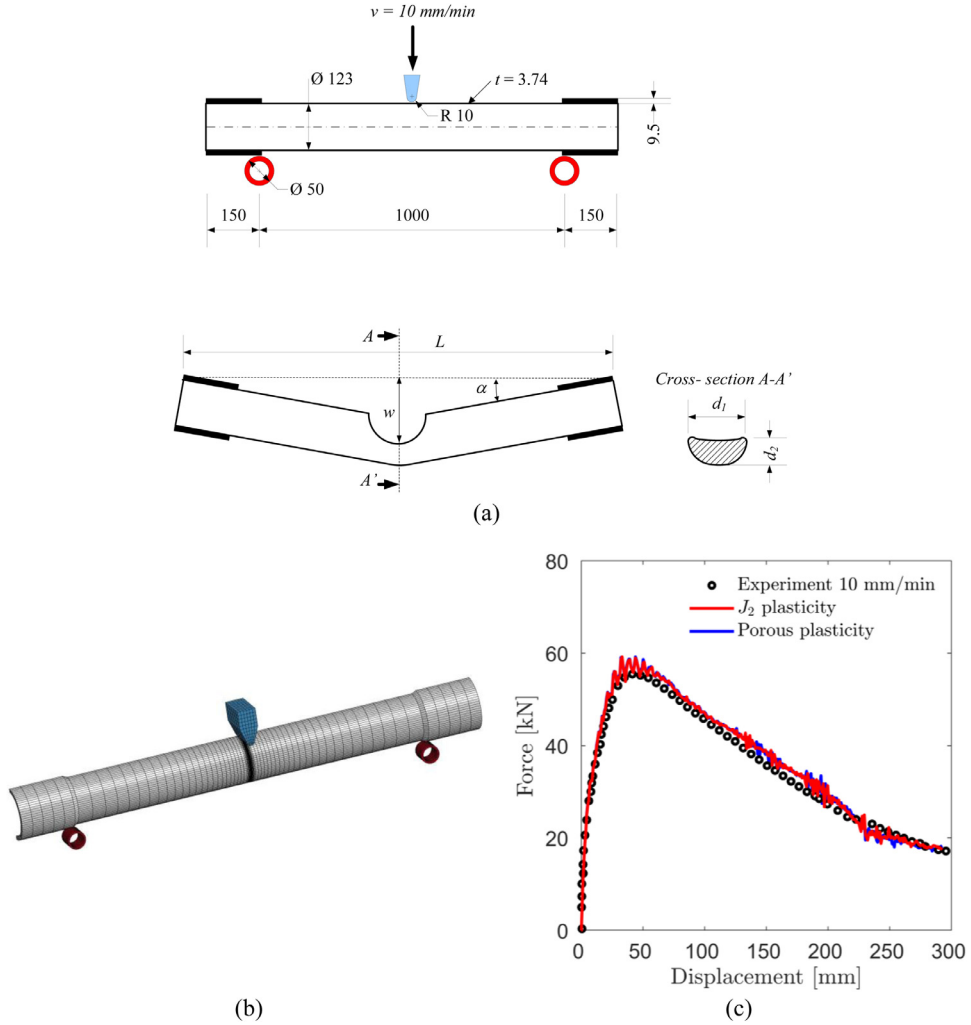

Fig. 7. (a) Geometry, dimensions in mm and testing conditions of the three-point pipe bending specimen ("Q2" from Kristoffersen et al. (2016b)) as well as its indented geometry. (b) Finite element model for the three-point pipe bending test. (c) Numerical simulations of quasi-static three-point pipe bending tests employing J2 (red) and porous plasticity (blue) models calibrated for the X65 pipe steel compared against the experimental data (hollow black circles) from Kristoffersen et al. (2016b).

against the experimental data in Fig. 7(c). The predictions of both models are in excellent agreement with the experimental force-displacement curve. The bifurcation indicator did not predict any onset of localisation for this particular test, which is in agreement with the observations reported in Kristoffersen et al. (2016b). However, it should be noted that the porous plasticity model was calibrated for an element size that corresponded to the tensile specimens. Therefore, even if the simulations are in agreement with the experimental observations, on must be cautious when analysing the results from the numerical simulations.

4. Finite element simulations of crease formation

Based on the numerical analysis performed by Yang et al. (2019), FE simulations of a plane-strain material block of dimensions $2L \times L$ with a symmetric quarter-circular imperfection with radius $R = L/1000$ as detailed in Fig. 8(a) were carried out. Employing the block's symmetry, only half was discretised with four-node reduced integration single-integration-point plane strain elements with stiffness-based hourglass control. Six elements were employed to discretise the contour of the artificial defect. To simulate the contact with the other half of the specimen, a rigid wall with no friction was employed as the symmetry plane. Since there are no experimental data to compare with, as a first approximation, the friction between contact surfaces was not considered. A prescribed horizontal displacement $u = u[t]$ was applied on the nodes located on the opposite edge to the symmetry plane, whereas the vertical displacement was constrained on the nodes located on the bottom edge. The prescribed displacement boundary conditions were obtained from assuming a constant applied velocity of $v = L \times 10^{-3}$[m/s]. The non-linear explicit time integration FE analysis solver LS-DYNA was employed to perform the numerical simulations. Mass scaled solutions with a stable time increment that required a minimum number of increments of no less than $2{\cdot}10^6$ were used.

The horizontal stretch $\lambda = l/L$ was used to measure the applied engineering strain, $e = \lambda - 1$, and the logarithmic strain, $\varepsilon = \ln[\lambda]$. The reference configuration at $t = 0$ and the current configuration at a time t of the symmetric FE model of the plane strain block are depicted in Fig. 8(b).

To ensure that the numerical set-up was properly defined, a J_2 plasticity model with a yield stress of $\sigma_y/E = 0.005$ was assigned to the block of material, which was compressed for three cases of bilinear work hardening with tangent moduli E_t/E of 0.1, 0.3 and 0.6. The normalised self-contact length a/L against the applied engineering strain was compared to the results from Yang et al. (2019) in Fig. 9. The numerical simulations performed with LS-DYNA applying the numerical set-up described

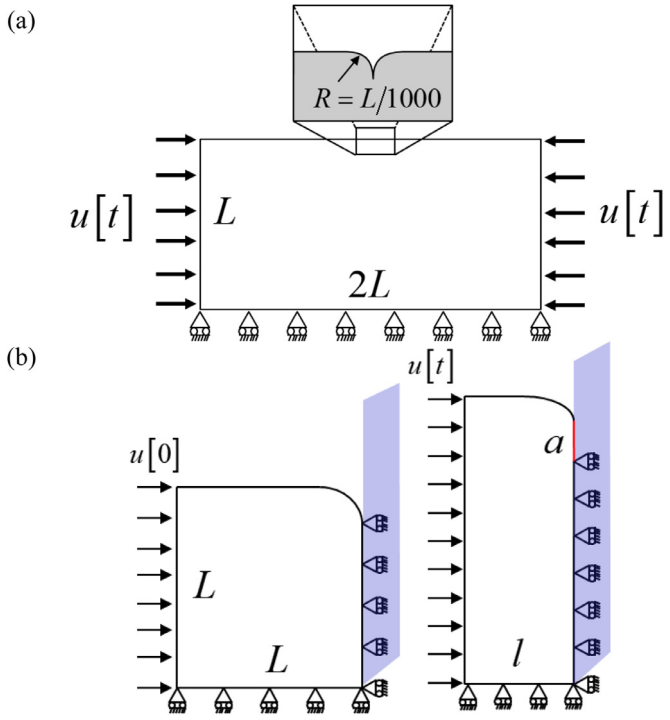

Fig. 8. (a) Schematic illustration of a plane-strain material block of $2L \times L$ that contains a symmetric quarter-circular imperfection of radius $R = L/1000$ on the top surface located at a distance L from the edges as shown in the detail. (b) Reference and current configurations of the symmetric half-block with an infinite rigid wall simulating the material self-contact.

Table 2
Tested specimen geometrical comparison between experiment ("Q2") from Kristoffersen et al. (2016b) and the numerical simulations performed with J_2 and Porous plasticity models.

Measurements	Experiment ("Q2")	J_2 plasticity	Porous plasticity
L[mm]	1042	1080.580	1080.550
w[mm]	380	345.054	345.514
d_1[mm]	202	203.970	203.870
d_2[mm]	26	21.093	21.091
α[°]	31	31.850	32.250

above were in excellent agreement with the results reported in Yang et al. (2019).

From Fig. 9, the critical strain e^c that characterises the crease formation can be easily determined as the applied strain that causes an unsteady growth of the self-contact length a. In other words, an abrupt increase in the self-contact length for a small increase in compressive strain. Therefore, from this figure two observations can be made: first, metals with stronger work hardening will form creases with lower applied compressive strains; and second, determining the critical strain in metals with weaker work hardening becomes progressively more and more difficult due to the lack of an abrupt transition between the stable and unstable self-contact growth. As an example, one can clearly observe the transition from stable to unstable self-contact growth in Fig. 9 for the cases where E_t/E is 0.6 and 0.3, where e^c is –0.43 and –0.57 respectively. However, for E_t/E equal to 0.1 it could be defined as a diffuse critical strain ranging from –0.74 to –0.80.

Table 2.

4.1. Compression-tension reverse straining simulations

To determine the critical strain e^c, simulations of the previously described block of material up to a minimum strain of –80% were performed for the X65 steel material. The simulations were carried

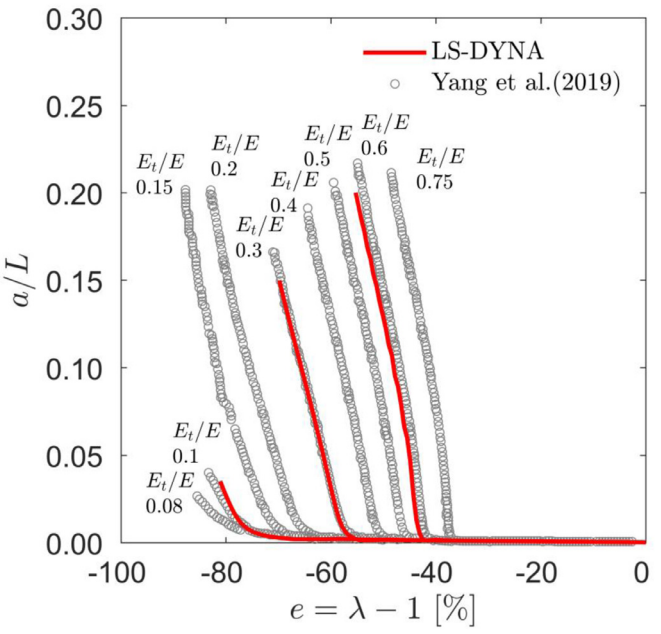

Fig. 9. Normalised self-contact length a/L against engineering strain e for a J_2 plasticity material with $\sigma_y/E = 0.005$. The hollow black points correspond to the results from Yang et al. (2019) and the red curves are obtained from the finite element simulations performed with the current numerical set-up in LS-DYNA. The numbers on top of the curves indicate the E_t/E values.

out using the Gurson porous plasticity model with the strain localisation indicator described in the previous sections along with the J_2 plasticity model for the sake of comparison. Four cases with minimum strains of –80%, –70%, –60% and –50% were studied. After the minimum strain was reached, the sign of the velocity was reversed and the blocks were strained under tension to analyse the influence of the defect created by the self-contact. Along with the horizontal stretch λ, the normalised reaction force per unit depth $F/(L\sigma_0)$, the normalised contact force per unit depth $F_{rw}/(L\sigma_0)$, the normalised self-contact length a/L, and the normalised major principal stress at the imperfection tip σ_I/σ_0 were monitored at all times.

Recall that the bifurcation condition ($\det[\mathbf{A}] = 0$) is used as an indicator of fracture initiation. Therefore, when bifurcation is detected we assume material fracture. These simulations will allow predicting when the self-contact defects created during the compression phase are catastrophic. However, there are certain limitations in the models employed in the numerical simulations that will be further discussed.

4.2. Results and discussion

Normalised reaction force per unit depth $F/(L\sigma_0)$ against engineering strain plots for minimum applied strains of –80%, –70%, –60% and –50% before strain reversal are shown in Fig. 10(a) and (b). Henceforth, unless stated otherwise, the plot with the red curves on the left (Fig. 10(a)) corresponds to the FE simulations carried out with the J_2 plasticity model and the blue curves on the right (Fig. 10(b)) correspond to those performed with the porous plasticity model. Despite largely exceeding the yield stress even for the lowest compressive strain (–50%), the combined volume fraction in the porous plasticity model during such a phase did not increase enough to soften the material behaviour. Although Gurson-like models do not explicitly produce material softening during compression phases, the previously mentioned anomalous behaviour exhibited by the combined volume fraction for this particular material could. The contact of the matrix material with

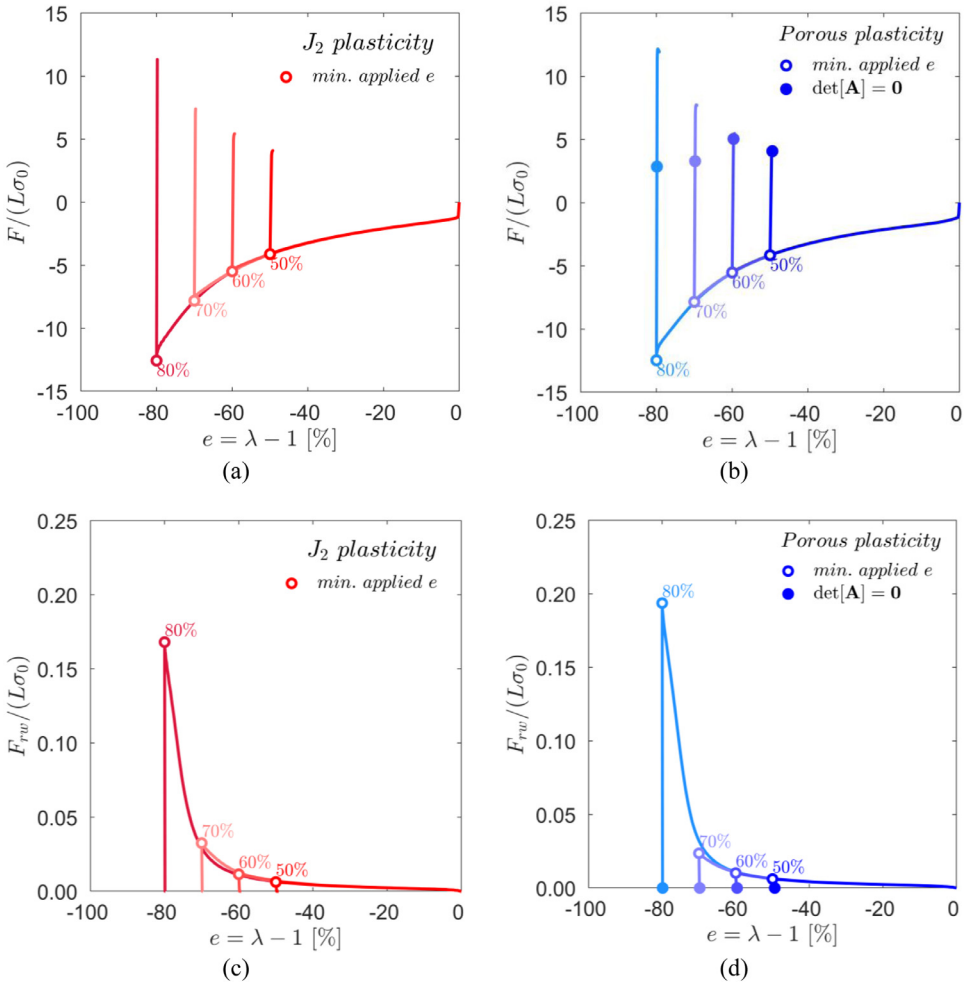

Fig. 10. Normalised reaction and contact forces F and F_{rw} respectively against the applied engineering strain e for J_2 plasticity in red (a-c, left) and for porous plasticity in blue (b-d, right). The hollow circles indicate the minimum applied engineering strain before it is reversed, and the solid blue circles signal localisation.

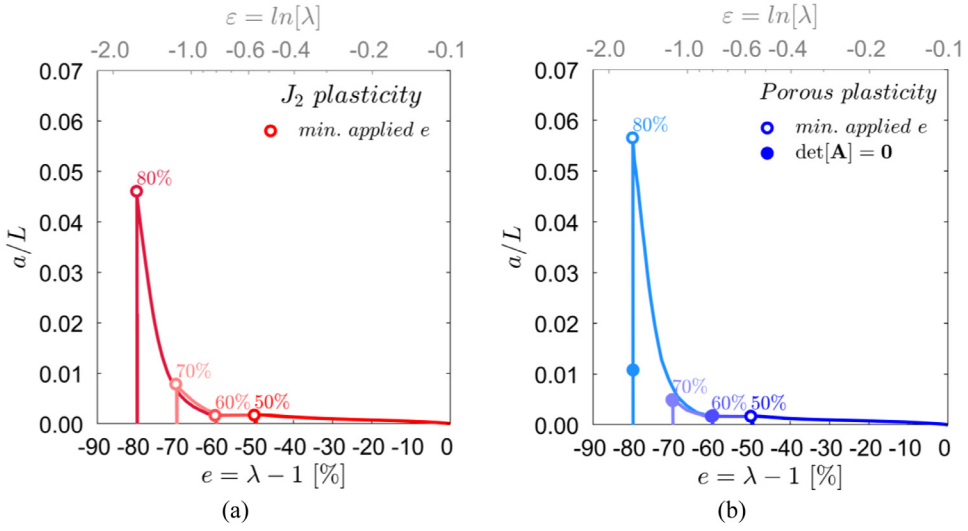

Fig. 11. Normalised self-contact length a/L against the applied engineering strain e logarithmic strain ε (top axis, grey) for J_2 plasticity in red (a) and for porous plasticity in blue (b). The hollow circles indicate the minimum applied engineering strain before it is reversed, and the solid blue circles signal localisation.

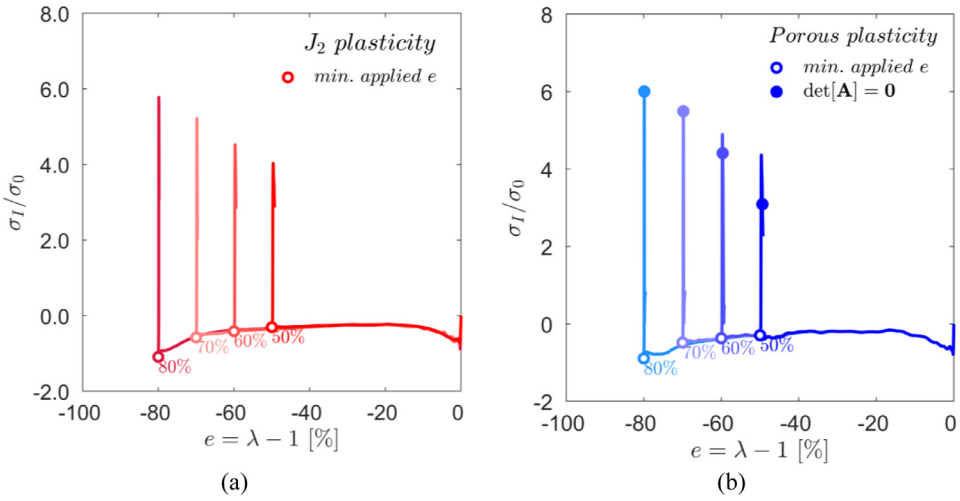

Fig. 12. Normalised major principal stress σ_I/σ_0 (σ_0 = 465.5MPa) against the applied engineering strain e for J_2 plasticity in red (a) and for porous plasticity in blue (b). The hollow circles indicate the minimum applied engineering strain before it is reversed, and the solid blue circles signal localisation.

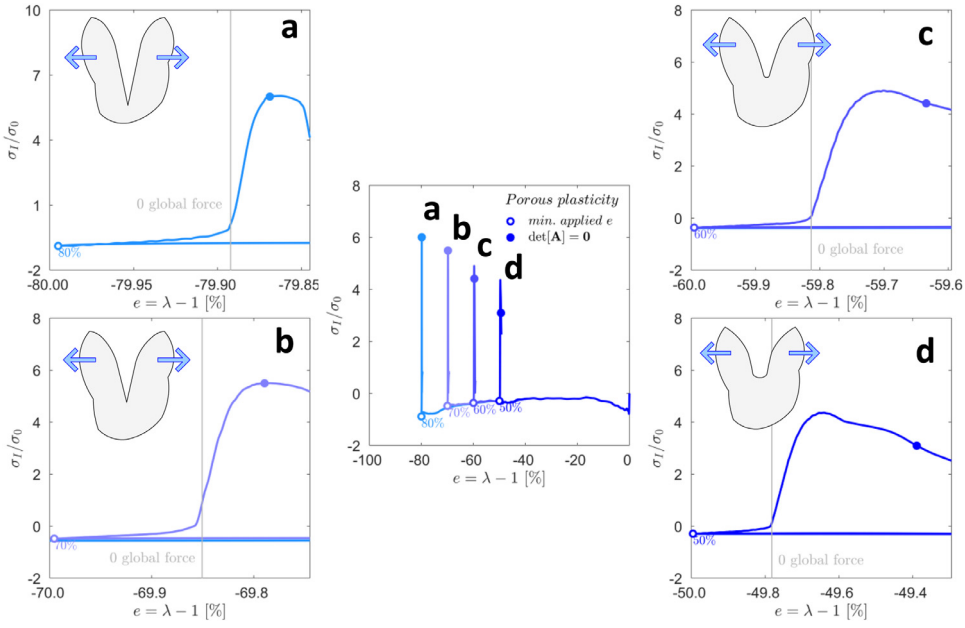

Fig. 13. Zoomed details of results obtained with the porous plasticity model normalised major principal stress σ_I/σ_0 against the applied engineering strain e plot for the cases with minimum applied strains of –80% (a), –70% (b), –60% (c) and –50% (d).

the particle embedded in it caused the combined volume fraction to increase with increasing compressive strains. However, further straining made this effect to fade, progressively converging towards a behaviour represented by a typical Gurson-like model. Both Fig. 10(a) and (b) present virtually identical responses during the compression phase. During the tensile phase, after the strain was reversed, the solid block was unloaded and then loaded back elastically until it plastified globally again. Further straining after this point showed some softening in the global response of the porous model. Interestingly, the localisation indicator predicted fracture initiation under global elastic loading for minimum applied strains of –80% and –70%, whereas for the minimum strain of –50% the fracture initiation was predicted above the global yielding point. The fracture initiation for the case of –60% applied strain was predicted in between the global elastic and plastic response of the solid block.

Normalised contact force per unit depth $F_{rw}/(L\sigma_0)$, that represents the self-contact force, against engineering strain plots for minimum applied strains before strain reversal of –80%, –70%, –60% and –50% are shown in Fig. 10(c) and (d). These curves represent the self-contact behaviour of the defect, and as such, they were able to indicate the steady-unsteady transition of the self-contact growth. It is clearly observed in these plots how the self-contact force grew very rapidly for small increases in compressive strains after 70%. Both models roughly predicted the same value. However, it was perhaps more difficult to clearly discern the appropriate value for the J_2 plasticity (Fig. 10(c)), whereas the porous plasticity model predicted a slight increase in the contact force with respect to the J_2 plasticity (Fig. 10(d)). This effect can be mainly attributed to the void growth in the porous plasticity model. For all cases, as expected, the fracture initiation was predicted after the self-contacting force ceased to exit, once the defect started to open. In summary, these curves could also be used to determine the critical strain for the onset of crease formation.

Normalised self-contact length a/L against engineering strain and their translation into logarithmic strain are shown in Fig. 11,

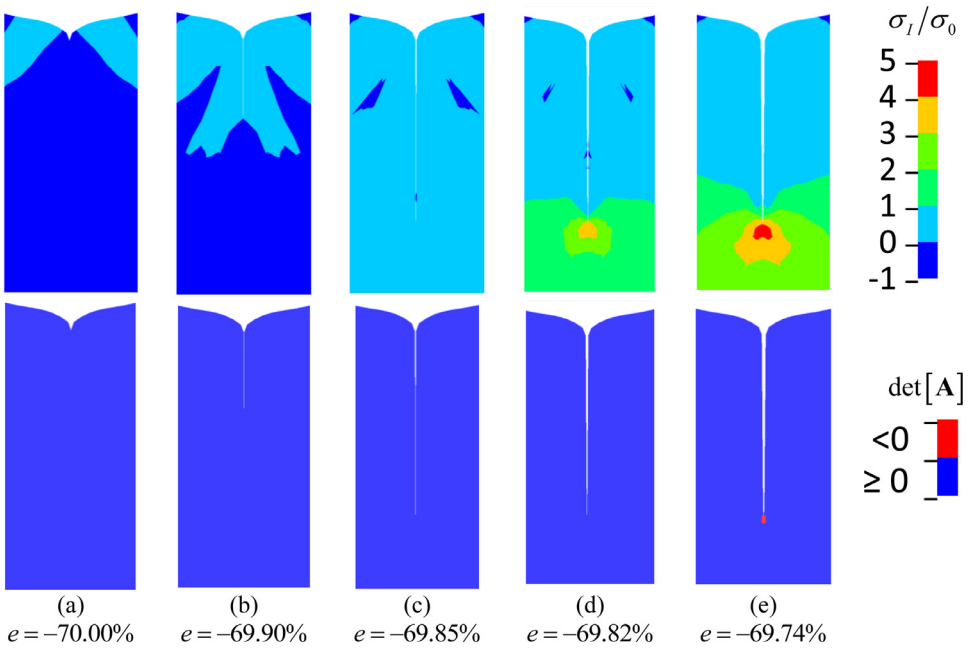

Fig. 14. Tensile straining phase image sequence until fracture initiation detection of the plane strain block FE simulation compressed at −70%. The top row contour plots show the normalised major principal stresses σ_I/σ_0, while the bottom row depicts binary contours of the failure indicator.

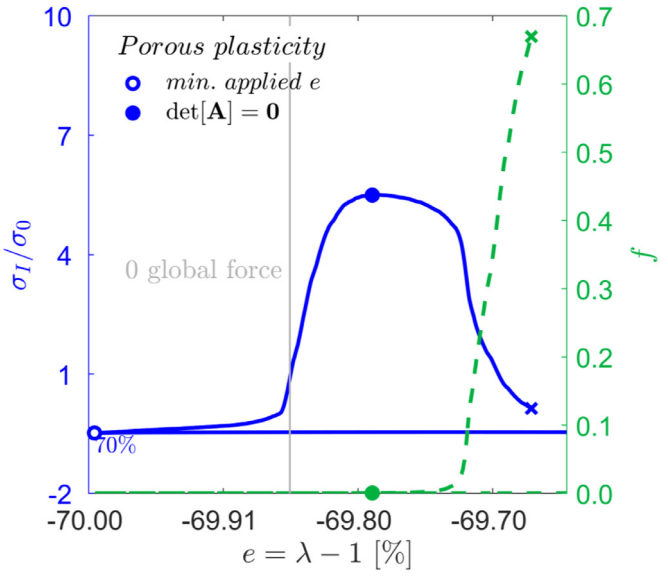

Fig. 15. Evolution of the normalised major principal stress σ_I/σ_0 and the combined volume fraction f gathered from the self-contacting defect tip during the tensile straining phase of the plane-strain block FE simulation compressed at −70%. The cross indicates that $f = 1/q_1$.

for minimum applied strains before strain reversal of –80%, –70%, –60% and –50%. The same conclusions as those extracted from the self-contact forces (see Fig. 10(c) and (d)) can be drawn from Fig. 11(a) and (b). However, the latter figures exhibited a slightly cleaner transition from steady to unsteady self-contact growth, being sharper for the porous plasticity model. From these, a critical strain of around $e^c \approx -70\%$ was estimated for both models. Fracture initiation was always detected in the tension phase after load reversal, clearly visible for the case of –80% of strain. However, for the rest of the cases the maximum and fracture self-contact length are very similar. For reference, Fig. 11(a) and (b) also show the self-contact length against the logarithmic strain, which can be more representative of the cases where a more local strain is measured such as diameter increase/reduction in round bars or local extensometers in flat specimens.

Normalised major principal stress σ_I/σ_0 against engineering strain plots for both models are shown in Fig. 12(a) and (b). The major principal stress at the tip of the defect during the compression phase was negative and progressively decreasing up to an engineering strain of –80%. After the strain was reversed, an acute increase of the major principal stress was observed changing the sign from negative to positive indicating that the previously created self-contact defect was pulled apart. In order to ascertain if the self-contact defect acted like a crack, zoomed in plots of the tensile straining phase of Fig. 12(b) are depicted in Fig. 13 for the minimum compression cases of –80% in (a), –70% in (b), –60% in (c) and –50% in (d). Two phases were identified in these plots: first, the unloading of the self-contact defect that seemed mostly horizontal, and second, the abrupt increase on the major principal stress until it reached a maximum value, followed by a progressive decrease attributed to the rounding of the self-contact defect tip. This, in turn, increased the combined volume fraction and locally softened the material. Once the crease was formed, this is around compressive strains of 70% and above, the localisation indicator predicted fracture initiation before the maximum major principal stress was reached, before any rounding and stretching at the tip of the defect occurred, as illustrated in Fig. 13(a) and (b). For the cases where the minimum applied strain was above –70%, the localisation indicator predicted fracture initiation way after the maximum major principal strain value was surpassed. In other words, for compressive strains below the critical strain, the tip of the self-contact defect was rounded off and stretched before fracture was detected. It should be remarked here that this is a first attempt to model the crease formation in steel materials and its effect on the ductile-to-brittle transition, and thus these results should be cautiously analysed. Typical mechanical responses of metallic materials, such as the Bauschinger effect, that can significantly affect the prediction of the fracture initiation were not taken into account. Such effect, that depends on the composition and microstructure of the metal in question, might either delay or promote the frac-

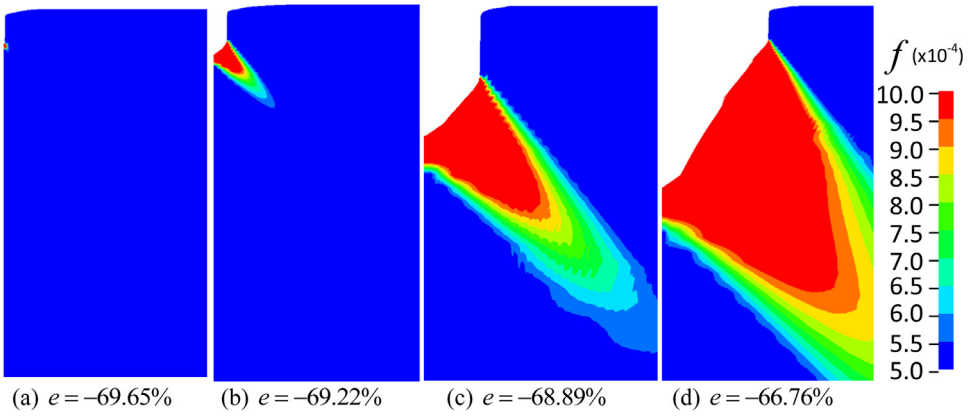

Fig. 16. Tensile straining phase image sequence showing combined volume fraction contours of the plane strain block FE simulation compressed at −70%, where $f = 1/q_1$ was used as an element erosion criterion.

ture initiation. However, it does not change the fact that a surface defect with a certain self-contact length has to be created during the compressive phase in order to induce a brittle failure when reversing the load.

Directly related to Fig. 13(b), Fig. 14 from (a) to (e) shows an image sequence corresponding to the tensile straining phase for the case of minimum applied strain of –70%. The top row shows contour plots of normalised major principal stresses σ_I/σ_0. The bottom row shows a binary contour where the blue colour represents values of the acoustic tensor larger than zero, i.e. $\det[\mathbf{A}] > 0$, and the red colour indicates values equal or less than zero, i.e. $\det[\mathbf{A}] \leq 0$. The onset of fracture, i.e. $\det[\mathbf{A}] = 0$, was first detected in the tip of the self-contact defect as it can be seen in Fig. 14. We can observe the unloading of the crack-like self-contact defect during the first phase of the curve shown in Fig. 13(b) from the images in Fig. 14(a) and (b). The opening of such defect, that can be correlated to the abrupt increase of the normalised major principal stress detected in Fig. 13(b), can be seen in the image sequence comprised by Fig. 14(c), (d) and (e).

To show the suitability of employing the bifurcation analysis as a fracture initiation criterion, the 70% compression case was simulated eroding the elements when the volume fraction reached $f = 1/q_1$, i.e. when the yield surface collapses. It should be noted that this value is taken as an extreme case for material failure. However, it should allow to estimate if the material fully collapses shortly after the fracture initiation is detected with $\det[\mathbf{A}] = 0$. Fig. 15 shows the evolution of the normalised major principal stress σ_I/σ_0 as well as the volume fraction f extracted from the tip of the self-contacting defect during the tensile straining phase. Once bifurcation was detected, the volume fraction increased rapidly deleting the element shortly after. Further straining caused the self-contacting defect to quickly open and caused the deletion of the elements located in front of such a defect as it is shown in Fig. 16. This adds confidence in the use of the bifurcation analysis as a fracture criterion.

5. Conclusions

The self-contacting defects created on the surface of largely compressed areas such as the compressive side on components subjected to bending actions in metals and their effect on the fracture mechanisms have been investigated. The self-contacting defects may evolve into creases when the former grow very rapidly for small increments of compressive strain, this is, unsteadily. To ascertain if the creasing phenomenon is involved in the ductile-to-brittle transition observed in metals that have been previously compressed, a finite element model of a half-space plane-strain block of material with an imperfection has been analysed. Experimentally validated associative J_2 and porous plasticity models have been used to model the mechanical response of a X65 pipe steel, chosen as the baseline material for this investigation. Additionally, a classical bifurcation analysis has been implemented via an user defined material subroutine along with the porous plasticity model. The loss of ellipticity indicator $\det[\mathbf{A}] = 0$ has been used as a fracture initiation criterion.

The finite element model of the material block has been compressed to 50%, 60%, 70% and 80% of its initial length and then tensile straining has been applied until the global non-linear tensile response has been amply surpassed. The onset of crease formation has been detected at a critical compressive applied strain of around 70%. Regardless of the compression level attained, self-contacting crack-like defects have been created. Of course, the defects vary in length being significantly larger for compressive strains above the critical strain. During the tensile phase, the bifurcation indicator detected fracture initiation at the tip of the self-contacting crack-like defects formed during the compressive state while they were still sharp for the cases compressed at 70% and 80%. However, for the rest of the cases, fracture initiation has been detected when the tip of the self-contacting crack-like defects have been rounded-off. Therefore, the crease formation seems to be closely linked to the decrease of ductility, or even ductile-to-brittle transitions, observed when these types of structural steels are largely compressed before they are subjected to load reversal. As mentioned in the results analysis, the predictions of the onset of fracture have to be taken cautiously since the Bauschinger effect was not explicitly accounted for in the material models employed in the finite element analyses.

Declaration of Competing Interest

The authors declare that they have no known competing financial interests or personal relationships that could have appeared to influence the work reported in this paper.

Acknowledgements

The present work has been carried out with financial support from Centre of Advanced Structural Analysis (CASA), Centre for Research-based Innovation, at the Norwegian University of Science and Technology (NTNU) and the Research Council of Norway through project no. 237885 (CASA).

References

Benallal, A., Comi, C., 1996. Localization analysis via a geometrical method. Int. J. Solids. Struct. 33, 99–119.

Budday, S., Andres, S., Walter, B., Steinmann, P., Kuhl, E., 2017. Wrinkling instabilities in soft bilayered systems. Philosophical Transactions of the Royal Society A: Mathematical. Phys. Eng. Sci. 375, 20160163.

Cao, Y., Hutchinson, J.W., 2012a. From wrinkles to creases in elastomers: the instability and imperfection-sensitivity of wrinkling. Proceedings of the Royal Society A: Mathematical. Phys. Eng. Sci. 468, 94–115.

Cao, Y., Hutchinson, J.W., 2012b. Wrinkling Phenomena in Neo-Hookean Film/Substrate Bilayers. J. Appl. Mech. 79.

Christoffersen, J., Hutchinson, J.W., 1979. A class of phenomenological corner theories of plasticity. J. Mech. Phys. Solids. 27, 465–487.

Dæhli, L.E.B., Børvik, T., Hopperstad, O.S., 2016. Influence of loading path on ductile fracture of tensile specimens made from aluminium alloys. Int. J. Solids. Struct 88–89, 17–34.

Faleskog, J., Gao, X., Shih, C.F., 1998. Cell model for nonlinear fracture analysis – I. Micromechanics calibration. Int. J. Fract. 89, 355–373.

Gent, A.N., Cho, I.S., 1999. Surface Instabilities in Compressed or Bent Rubber Blocks. Rubber. Chem. Technol. 72, 253–262.

Gurson, A.L., 1977. Continuum Theory of Ductile Rupture by Void Nucleation and Growth - Part I: yield Criteria and Flow Rule. J. Eng. Mater. Technol 99, 2–15.

Hohlfeld, E., Mahadevan, L., 2012. Scale and Nature of Sulcification Patterns. Phys. Rev. Lett. 109, 025701.

Hong, W., Zhao, X., Suo, Z., 2009. Formation of creases on the surfaces of elastomers and gels. Appl. Phys. Lett. 95, 111901.

Hutchinson, J.W., Tvergaard, V., 1980. Surface instabilities on statically strained plastic solids. Int. J. Mech. Sci. 22, 339–354.

Jin, L., Cai, S., Suo, Z., 2011. Creases in soft tissues generated by growth. EPL (Europhysics Lett.) 95, 64002.

Kristoffersen, M., 2014. Impact Against X65 Offshore Pipelines. Department of Structural Engineering. Norwegian University of Science and Technology (NTNU).

Kristoffersen, M., Børvik, T., Hopperstad, O.S., 2016a. Using unit cell simulations to investigate fracture due to compression–tension loading. Eng. Fract. Mech. 162, 269–289.

Kristoffersen, M., Børvik, T., Langseth, M., Hopperstad, O.S., 2016b. Dynamic versus quasi-static loading of X65 offshore steel pipes. Eur. Phys. J. Spec. Top. 225, 325–334.

Kristoffersen, M., Børvik, T., Westermann, I., Langseth, M., Hopperstad, O.S., 2013. Impact against X65 steel pipes – An experimental investigation. Int. J. Solids. Struct. 50, 3430–3445.

Kristoffersen, M., Casadei, F., Børvik, T., Langseth, M., Hopperstad, O.S., 2014. Impact against empty and water-filled X65 steel pipes – Experiments and simulations. Int. J. Impact. Eng. 71, 73–88.

Legarth, B.N., Richelsen, A.B., 2006. Surface instabilities during straining of anisotropic materials. Int. J. Mech. Sci. 48, 517–525.

Li, B., Cao, Y.-.P., Feng, X.-.Q., 2011a. Growth and surface folding of esophageal mucosa: a biomechanical model. J. Biomech. 44, 182–188.

Li, B., Cao, Y.-.P., Feng, X.-.Q., Gao, H., 2011b. Surface wrinkling of mucosa induced by volumetric growth: theory, simulation and experiment. J. Mech. Phys. Solids. 59, 758–774.

Lihua, J., 2014. Mechanical Instabilities of Soft Materials: Creases, Wrinkles, Folds, and Ridges. Harvard University.

Mora, S., Abkarian, M., Tabuteau, H., Pomeau, Y., 2011. Surface instability of soft solids under strain. Soft. Matter. 7, 10612–10619.

Morin, D., Hopperstad, O.S., Benallal, A., 2018. On the description of ductile fracture in metals by the strain localization theory. Int. J. Fract. 209, 27–51.

Oliver, J., Huespe, A.E., 2004. Theoretical and computational issues in modelling material failure in strong discontinuity scenarios. Comput. Methods. Appl. Mech. Eng. 193, 2987–3014.

Rice, J.R., 1976. Localization of Plastic Deformation.. Brown Univ., Providence, R.I. (USA). Div. of Engineering.

Rice, J.R., Rudnicki, J.W., 1980. A note on some features of the theory of localization of deformation. Int. J. Solids. Struct. 16, 597–605.

Rudnicki, J.W., Rice, J.R., 1975. Conditions for the localization of deformation in pressure-sensitive dilatant materials. J. Mech. Phys. Solids. 23, 371–394.

Stewart, P.S., Waters, S.L., El Sayed,, T., Vella, D., Goriely, A., 2016. Wrinkling, creasing, and folding in fiber-reinforced soft tissues. Extreme. Mech. Lett. 8, 22–29.

Triantafyllidis, N., Needleman, A., Tvergaard, V., 1982. On the development of shear bands in pure bending. Int. J. Solids. Struct. 18, 121–138.

Trujillo, V., Kim, J., Hayward, R.C., 2008. Creasing instability of surface-attached hydrogels. Soft. Matter. 4, 564–569.

Tvergaard, V., 1981. Influence Of Voids On Shear Band Instabilities Under Plane-Strain Conditions. Int. J. Fract. 17, 389–407.

Yang, J., Jin, L., Hutchinson, J.W., Suo, Z., 2019. Plasticity retards the formation of creases. J. Mech. Phys. Solids. 123, 305–314.

Yoon, J., Kim, J., Hayward, R.C., 2010. Nucleation, growth, and hysteresis of surface creases on swelled polymer gels. Soft. Matter. 6, 5807–5816.